

Cite this: *Green Chem.*, 2019, **21**, 4443

# Ammonia photosynthesis *via* an association pathway using a plasmonic photoanode and a zirconium cathode†

Tomoya Oshikiri, <sup>a</sup> Kosei Ueno<sup>‡a</sup> and Hiroaki Misawa <sup>\*a,b</sup>

Most conventional photoelectrochemical-based methods for synthesizing  $\text{NH}_3$  show low selectivity due to the generation of  $\text{H}_2$  as a by-product. In principle, two types of reaction mechanisms can occur in the reduction of  $\text{N}_2$  to  $\text{NH}_3$ . One is an associative pathway in which  $\text{N}_2$  molecules on the catalyst are hydrogenated. The other is a dissociative pathway in which nitrogen and hydrogen react after the cleavage of the strong  $\text{N}_2$  triple bond. Understanding the mechanism of  $\text{NH}_3$  formation on the electrode will facilitate the development of selective and efficient  $\text{NH}_3$  synthesis techniques. In this study, we constructed a two-electrode system composed of a strontium titanate photocatalytic anode in which the plasmon effect is expressed by plasmonic gold nanoparticles and a zirconium cathode, which was connected to the external circuit to investigate the reaction by electrochemical analysis in addition to analysis of the product. The bias and pH dependences of the reaction were then systematically investigated, and the plasmon-induced synthesis of  $\text{NH}_3$  on Zr was proposed to proceed *via* an associative pathway.

Received 17th May 2019,

Accepted 8th July 2019

DOI: 10.1039/c9gc01658a

rsc.li/greenchem

## Introduction

Ammonia ( $\text{NH}_3$ ) has attracted considerable attention as a hydrogen carrier and combustion fuel in addition to being a key precursor of synthetic fertilizer.<sup>1–3</sup>  $\text{NH}_3$  is industrially produced by the Haber–Bosch process, which involves the heterogeneous reaction of  $\text{N}_2$  and  $\text{H}_2$  produced from fossil fuels under harsh conditions at high pressure (20 MPa) and temperature (400 °C).<sup>4–6</sup> Although researchers have attempted to synthesize  $\text{NH}_3$  under milder conditions by improving the thermochemical catalyst,<sup>7,8</sup> the cleavage of the  $\text{N}_2$  triple bond still requires high energy. Therefore, another approach that produces  $\text{NH}_3$  with low energy consumption, such as an enzymatic method, is needed if  $\text{NH}_3$  is to be used as an energy carrier.

Previously, numerous efforts have been devoted towards developing electrochemical<sup>9–12</sup> and photocatalytic<sup>13–17</sup> methods for synthesizing  $\text{NH}_3$  under ambient conditions. However, most of these synthetic methods show low selectivity due to the formation of  $\text{H}_2$  as a by-product. Additionally, in

particular, it is difficult that a semiconductor photocatalyst utilizes a broadband solar spectrum is difficult because of the band structure limitations. Plasmon-related photoreactions are expected to be a novel way to utilize the visible and near-infrared light in the solar spectrum because of the light harvesting properties.<sup>18–23</sup> Recently, we reported that  $\text{NH}_3$  was selectively synthesized through the reduction of nitrogen using water as the electron source by using strontium titanate ( $\text{SrTiO}_3$ ) loaded with gold nanoparticles (Au-NPs) on one side and zirconium (Zr) on the other side.<sup>24,25</sup> The reaction was driven *via* plasmon-induced charge separation on the Au-NP-loaded  $\text{SrTiO}_3$  photoanode, and Zr served as the cathode and co-catalyst. The proposed mechanism of plasmon-induced water oxidation is described below.<sup>26</sup> The hot-electron in the plasmonic metal nanoparticles is excited through the decay of the localized surface plasmon resonance (LSPR). A hole with a high oxidation ability remained at the surface states of the semiconductor near the metallic nanoparticle, and this hole has the potential to photocatalytically oxidize water.<sup>26,27</sup> However, the mechanism of nitrogen reduction, such as electron flow, that is active in  $\text{NH}_3$  production on the cathode is still unclear because the conventional plasmonic  $\text{NH}_3$  synthesis system, which integrates both the anode and cathode into one substrate, did not provide electrochemical information including the photocurrent flow and potential differences between the anode and cathode.

In this study, we constructed a two-electrode system connected to an external circuit to investigate the reaction by electrochemical analysis in addition to product analysis. We

<sup>a</sup>Research Institute for Electronic Science, Hokkaido University, Sapporo 001-0021, Japan. E-mail: misawa@es.hokudai.ac.jp; Tel: +81-11-706-9358; Fax: +81-11-706-9359

<sup>b</sup>Center for Emergent Functional Matter Science, National Chiao Tung University, Hsinchu 30010, Taiwan

†Electronic supplementary information (ESI) available. See DOI: 10.1039/c9gc01658a

‡The present address of Prof. K. Ueno is Department of Chemistry, Faculty of Science, Hokkaido University, Sapporo 060-0810 (Japan).

also investigated the effect of the bias and pH on the plasmon-induced  $\text{NH}_3$  synthesis on Zr.

## Results and discussion

### Construction of plasmon-induced $\text{NH}_3$ synthesis device

Fig. 1a shows the SEM image and extinction spectrum of the Au-NPs decorated on the  $\text{SrTiO}_3$  substrate in air. The average size of the Au-NPs is 45 nm, and the LSPR band exhibited a maximum at approximately 600 nm. Also, the cross-sectional image showed that the Au-NP has the hemispherical shape. The  $\text{SrTiO}_3$  loaded with Au-NPs (Au-NPs/ $\text{SrTiO}_3$ ) as a plasmonic photoanode was connected to the Zr coil as a cathode through the electrochemical analyser, as shown in Fig. 1b. Although the surface of metallic Zr is oxidized by  $\text{O}_2$  under ambient conditions, the oxidized surface is chemically stable for a long period.<sup>25</sup> Additionally, the thickness of the oxide layer should decrease under cathodic conditions.<sup>28</sup> The anodic and cathodic chambers were separated by an ion exchange film, and  $\text{N}_2$  was continuously bubbled through the cathodic chamber during the reaction. Although the cathodic chamber was not sealed, a contamination of ambient air was prevented by the continuous  $\text{N}_2$  flow. The two-electrode system used a similar circuit with the  $\text{SrTiO}_3$  electrode loaded with Au-NPs on one side and Zr on the other side<sup>25</sup> except an ion exchange membrane served as an efficient proton transport path, as shown in Fig. 1c and d. For the measurement of evolved  $\text{H}_2$ , a sealed cell in which  $\text{N}_2$  was encapsulated in the chamber (Fig. S1a†) was employed.

### Photoelectrochemical measurements on plasmon-induced $\text{NH}_3$ synthesis

Fig. 2a depicts the current density and voltage ( $J$ - $V$ ) characteristics of the two-electrode system using a  $\text{SrTiO}_3$  photoanode

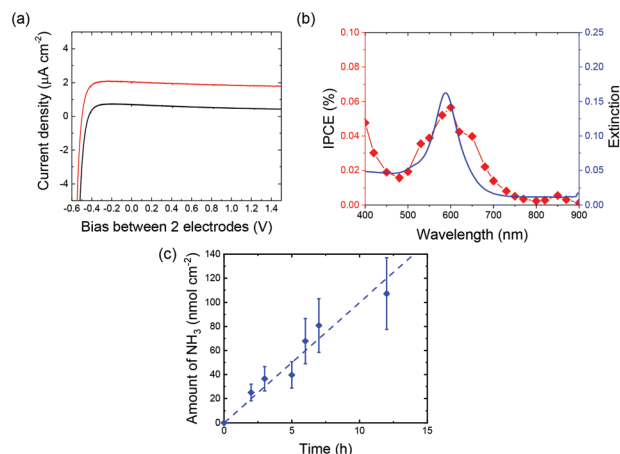


**Fig. 2**  $J$ - $V$  characteristics (a), IPCE action spectrum (b), and amount of  $\text{NH}_3$  formed (c) with the two-electrode system using a Au-NPs/ $\text{SrTiO}_3$ |Zr coil. The red and black lines indicate the current under irradiation and dark conditions, respectively. The applied biases were 0 and 1.0 V for the IPCE and  $\text{NH}_3$  measurements, respectively. The irradiation wavelength was 410–810 nm for the  $J$ - $V$  and  $\text{NH}_3$  measurements.

loaded with Au-NPs and a Zr coil cathode (Au-NPs/ $\text{SrTiO}_3$ |Zr coil). A good rectification property derived from the  $\text{SrTiO}_3$  was observed in dark conditions. Additionally, a stable photocurrent was observed under visible light irradiation over a wide range of applied biases. The photocurrent is derived from hot-electron-induced charge separation due to LSPR excitation because the action spectrum of the incident photon-to-current efficiency (IPCE) corresponds to the plasmon resonance spectrum, as shown in Fig. 2b, and the  $\text{SrTiO}_3$  does not absorb visible light longer than 390 nm.

Fig. 2c shows the amount of  $\text{NH}_3$  evolved in the cathodic chamber as a function of irradiation time with visible light (410–800 nm) with an applied bias of 1.0 V. The amount of  $\text{NH}_3$  formed under visible light irradiation on the  $\text{SrTiO}_3$  loaded with Au-NPs linearly increased with increasing irradiation time, and the rate of  $\text{NH}_3$  formation was 10  $\text{nmol h}^{-1} \text{cm}^{-2}$ . This rate is approximately 10 times larger than the reported with plasmonic ammonia synthesis systems.<sup>25</sup> The larger reaction rate of  $\text{NH}_3$  photosynthesis was achieved due to the efficient ion transport path, the greater cathode surface area, and the continuous supply of  $\text{N}_2$  gas.

### Bias and pH dependence of plasmon-induced $\text{NH}_3$ synthesis

In principle, two types of reaction mechanisms are possible in the reduction of  $\text{N}_2$  to  $\text{NH}_3$ , as shown in Fig. 3.<sup>29</sup> One is an associative pathway in which  $\text{N}_2$  molecules on the catalyst are hydrogenated.<sup>30</sup> The other is a dissociative pathway in which nitrogen and hydrogen react after the cleavage of the strong  $\text{N}_2$  triple bond.<sup>31</sup> Enzymes such as nitrogenase follow the associative pathway as the activation energy is lower. However, the Haber-Bosch method uses the dissociative pathway. Understanding the reaction mechanism of  $\text{NH}_3$  formation on Zr will facilitate the development of selective and efficient  $\text{NH}_3$  synthesis techniques. Therefore, the effects of the applied potential and concentration

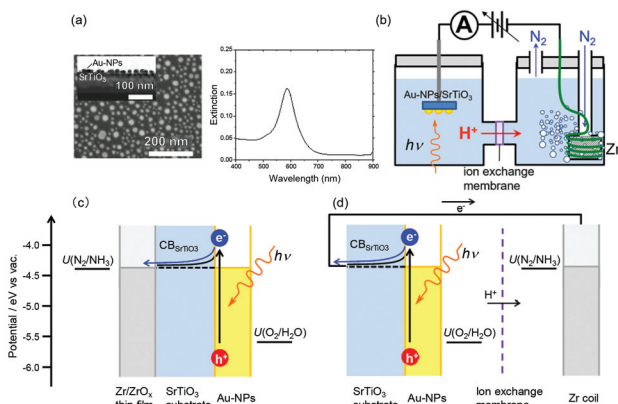


**Fig. 1** (a) SEM image and extinction spectrum of Au-NPs on  $\text{SrTiO}_3$ . An inset figure shows the cross-sectional scanning transmission electron microscopy (STEM) image of Au-NPs on  $\text{SrTiO}_3$ . (b) Schematic of the reaction cell. (c, d) Energy level diagrams of the  $\text{SrTiO}_3$  electrode loaded with Au-NPs on one side and Zr on the other side (c) and the two-electrode system using Au-NPs/ $\text{SrTiO}_3$  and Zr. The redox potentials  $U(\text{N}_2/\text{NH}_3)$  and  $U(\text{O}_2/\text{H}_2\text{O})$  were obtained from the literature.<sup>28,29</sup>



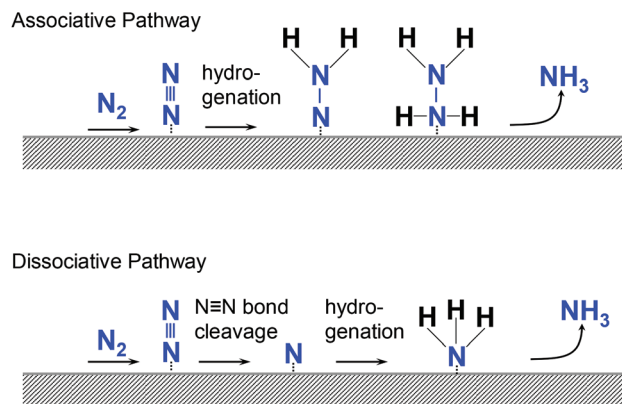


Fig. 3 Generic mechanisms for  $\text{N}_2$  reduction to  $\text{NH}_3$  on heterogeneous catalysts.

of reactants on the reaction are important. Fig. 4a shows the faradaic efficiency (FE) of  $\text{NH}_3$  formation calculated from the amount of  $\text{NH}_3$  formed and the photocurrent as a function of the applied bias. Hydrazine ( $\text{N}_2\text{H}_4$ ) was also measured by the colorimetric method because  $\text{N}_2\text{H}_4$  is a possible intermediate in  $\text{NH}_3$  production through the associative pathway.<sup>12,32</sup>

When the applied bias is small, no  $\text{NH}_3$  was detected. A small amount of  $\text{NH}_3$  was observed with an applied bias of

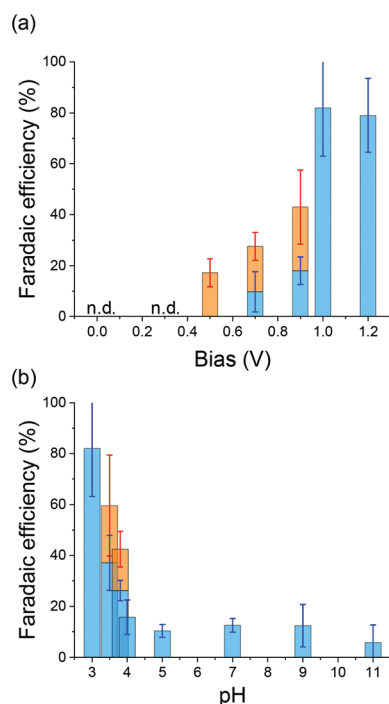


Fig. 4 FEs for  $\text{NH}_3$  and  $\text{N}_2\text{H}_4$  in the two-electrode system using a Au-NPs/SrTiO<sub>3</sub>/Zr coil as a function of the applied bias (a) and pH (b). The pH of the solution was fixed at 3 when determining bias dependence. The applied bias was fixed at 1.0 V when determining the pH dependence. The irradiation wavelength was 410–800 nm. The blue and orange bars indicate the FEs of  $\text{NH}_3$  and  $\text{N}_2\text{H}_4$ , respectively. The value less than the detection limit is represented as not determined (n.d.).

0.7 V. The FE of  $\text{NH}_3$  increased as the applied bias increased, reaching approximately 80% when the applied bias was 1.0 V. Additionally,  $\text{N}_2\text{H}_4$  was observed when the applied bias was from 0.5 to 0.9 V. To understand the applied potential on the cathode in well-defined condition, the three-electrode electrochemical reaction was performed using Zr as the working electrode. The current-voltage characteristics of Zr under  $\text{N}_2$  ( $I_{\text{N}_2}$ ) and Ar ( $I_{\text{Ar}}$ ) bubbling conditions and the current enhancement by  $\text{N}_2$  calculated as  $(I_{\text{N}_2} - I_{\text{Ar}})/I_{\text{N}_2}$  under dark conditions are shown in Fig. S2.†  $I_{\text{N}_2}$  is larger than  $I_{\text{Ar}}$  over a wide range of applied potentials, and the current enhancement showed a maximum at  $-0.3$  V vs. Ag/AgCl of the applied bias.

Fig. 4b depicts the FEs of  $\text{NH}_3$  and  $\text{N}_2\text{H}_4$  as a function of pH under an applied bias of 1.0 V. It was confirmed that the pH was not increased during the reaction (Fig. S3†). The FE of  $\text{NH}_3$  was very poor when the pH was larger than 4.0. However, the FE of  $\text{NH}_3$  increased dramatically as the pH decreased below 4.0. In contrast,  $\text{N}_2\text{H}_4$  was observed when the pH was between 3.5 and 4.0. This result indicates that the proton concentration directly affects  $\text{NH}_3$  production.

Notably, both the bias and pH dependencies indicate that intermediate values of bias and pH produce  $\text{N}_2\text{H}_4$ . These results suggest that reaction acceleration is needed for  $\text{NH}_3$  production, and  $\text{N}_2\text{H}_4$  may be an intermediate in  $\text{NH}_3$  production. However, the reduction potential from  $\text{N}_2$  to  $\text{N}_2\text{H}_4$  ( $-0.33$  V vs. the reversible hydrogen electrode (RHE)) is negative relative to that from  $\text{N}_2$  to  $\text{NH}_3$  ( $0.09$  V vs. RHE).<sup>32</sup> Therefore, plasmon-induced  $\text{NH}_3$  formation *via* a six-electron and six-proton transfer process on Zr proceeded kinetically rather than thermodynamically. Also, there is a possibility that the produced  $\text{N}_2\text{H}_4$  was consumed as a redox reagent due to the high reduction ability.<sup>33</sup> Additionally, the sum of the FEs of  $\text{NH}_3$  and  $\text{N}_2\text{H}_4$  does not equal 100% in the intermediate region. One of the other electron-consuming processes is the self-reduction of the Zr surface, and the other process is  $\text{H}_2$  production *via* proton reduction.  $\text{H}_2$  production was evaluated by using a sealed reaction cell. As a result, approximately 50% of the photocurrent was used for proton reduction under the applied bias of 0.7 V (Fig. S1b†). Also, the FE of  $\text{H}_2$  was less than detection limit under the applied bias of 1.0 V.

### Proposed reaction mechanism

In previous reports using isotopic reactants, water oxidation on the plasmonic photoanode and  $\text{NH}_3$  evolution by  $\text{N}_2$  reduction on the Zr cathode proceeded *via* plasmon-induced  $\text{NH}_3$  synthesis.<sup>19,25</sup> In particular, it was predicted that  $\text{N}_2$  is reduced by proton addition in the aqueous solution rather than the addition of a hydrogen adatom.

Based on the results described above, we propose the plasmon-induced  $\text{NH}_3$  synthesis on Zr proceeds *via* an associative pathway in which  $\text{N}_2$  is hydrogenated by protons (Fig. 5). Initially, the  $\text{N}_2$  molecule is preferentially adsorbed on the Zr surface (step i).<sup>34,35</sup> Subsequently, the reduction of  $\text{N}_2$  proceeds *via* proton addition (step ii) because the hypothesis that protons attach to the adsorbed  $\text{N}_2$  is supported by the depen-



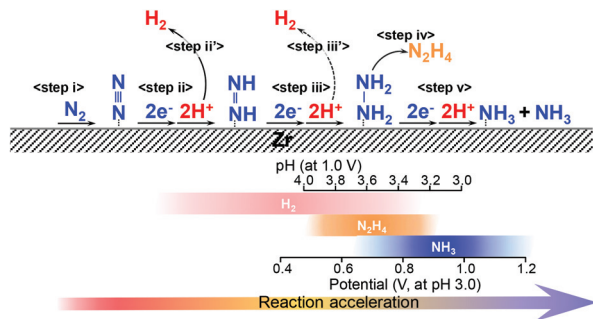


Fig. 5 A possible reaction pathway of  $\text{NH}_3$  formation on Zr.

dence of the  $\text{NH}_3$  production on the proton concentration, as shown in Fig. 3b. When the pH was large and applied potential was low,  $\text{H}_2$  was also produced as a by-product (step ii', iii'). Additionally, when the applied potential and proton concentration are moderate (pH 3.5–4.0 at applied bias of 1.0 V, or applied bias 0.5–0.9 V at pH 3.0),  $\text{N}_2\text{H}_4$  is produced as the major product *via* a four-electron transfer process (step iii–iv). If the reaction rate is high enough with a large applied bias and a high proton concentration,  $\text{NH}_3$  is produced as the main product *via* a six-electron transfer process (step v). We conclude that the reason for the high selectivity in  $\text{N}_2$  conversion on Zr is due to the association process without direct cleavage of the strong  $\text{N}_2$  triple bond.

## Experimental

### Preparation of plasmonic photoanode

Au-NPs/SrTiO<sub>3</sub> photoanode was fabricated according to the previous reports.<sup>19</sup> The Au-NPs/SrTiO<sub>3</sub> photoelectrode was fabricated by Helicon sputtering (ULVAC, MPS-4000C1/HC1) of 3 nm Au film on a single crystal of 0.05 wt% Nb-doped SrTiO<sub>3</sub> ( $10 \times 10 \times 0.5 \text{ mm}^3$ , Furuuchi Chemical) with a (110) surface, and subsequent annealing at 800 °C in  $\text{N}_2$ . The morphology of Au-NPs on the SrTiO<sub>3</sub> was observed using field-emission scanning electron microscopy (FE-SEM, JSM-6700FT, JEOL); the maximum resolution attainable at an electron acceleration voltage of 15 kV was 1 nm. The cross-sectional structure of the Au-NPs/SrTiO<sub>3</sub> was observed by STEM (Hitachi HD-2000 operated at 200 kV). The cross-sectional STEM sample was prepared using the focused ion beam technique (JEOL JIB-4600F/HKD) with Ga ions.

### Photoelectrochemical reaction

The  $\text{N}_2$  fixation device comprised reaction cells with two reaction chambers separated by the Nafion® 117 proton exchange membrane (Aldrich). An InGa alloy (2 : 1 weight ratio) film was pasted onto the backside of the plasmonic photoanode and then connected to an electrochemical analyzer (ALS/CH Instruments 760DH (ALS)) as a photoanode with a copper lead wire. A Zr coil was used as a cathode. The surface area of the Zr coil was  $0.628 \text{ cm}^2$ . An  $\text{H}_2\text{SO}_4$  aqueous solution (pH 3) was

filled in both chambers as the supporting electrolyte solution without any specific electron donor, and the  $\text{N}_2$  was bubbled in the cathodic chamber with 50 sccm during the reaction. When the pH of the solution was less than 4, the concentration of the electrolyte was kept as  $0.05 \text{ mol dm}^{-3}$  by the addition of  $\text{Na}_2\text{SO}_4$ . The photoanode was irradiated in an area of  $\varnothing 6 \text{ mm}$  ( $0.283 \text{ cm}^2$ ) by a xenon lamp (800 W, Newport) using an arbitrary light intensity and wavelength, and the amount of  $\text{NH}_3$  formed per area was calculated by dividing the value by the irradiation area. For the IPCE calculation, the photocurrent was measured at 0 V between two-electrode. The IPCE was calculated by the following equation:

$$\text{IPCE} = \frac{1240 \cdot J(\text{A cm}^{-2})}{\lambda(\text{nm}) \cdot P(\text{W cm}^{-2})} \times 100\%$$

where  $J$  is the photocurrent density generated by monochromatic light with a bandwidth of less than 15 nm,  $\lambda$  is the wavelength of the monochromatic incident light, and  $P$  is the light intensity. Bandpass filters with a bandwidth of less than 15 nm at the full-width at half-maximum were used.

The FEs of  $\text{NH}_3$  and  $\text{N}_2\text{H}_4$  were calculated by the following equation:

$$\text{FE} = \frac{n \cdot N(\text{mol}) \cdot F(\text{C mol}^{-1})}{Q(\text{C})} \times 100\%$$

where  $N$  is the amount of the generated products in the process,  $F$  is the faradaic constant,  $96485 \text{ C mol}^{-1}$ ,  $n$  is the number of electrons involved in the reaction,  $Q$  is the total charge passed through the whole reaction.

### Assays

The quantity of  $\text{NH}_3$  formed and evolved  $\text{H}_2$  were determined using the procedure using sodium salicylate, pyrazole, sodium hypochlorite, and sodium hydroxide.<sup>25</sup> We passed 0.5 mL of deionized water through the cathodic chamber to fully dissolve the  $\text{NH}_3$  (gas phase) and  $\text{NH}_4\text{Cl}$  (aqueous solution) formed. After the solution was neutralized to pH 7 using a  $1.5 \text{ mol dm}^{-3}$  sodium hydroxide aqueous solution, the following materials were added successively; 0.08 mL of an aqueous solution of ethylenediaminetetraacetic acid tetrasodium salt hydrate ( $1.3 \text{ mol dm}^{-3}$ ); 0.16 mL of an aqueous solution of sodium salicylate ( $1.46 \text{ mol dm}^{-3}$ ) and pyrazole ( $0.24 \text{ mol dm}^{-3}$ ); 0.52 mL of an aqueous solution of sodium hydroxide ( $1.25 \text{ mol dm}^{-3}$ ) and sodium hypochlorite ( $0.25 \text{ mol dm}^{-3}$ ). The sodium salicylate formed a dimer in the presence of  $\text{NH}_3$  with absorption at  $\lambda_{\text{max}} = 650 \text{ nm}$ . Ammonium chloride was purchased (Wako chemical, LTD) and used for calibration. The absorption spectra were monitored using a UV/vis spectrometer (UV-3100, Shimadzu). The value for  $\text{NH}_3$  formation at 0 hours was subtracted from all of the data as the background.

The quantity of formed  $\text{N}_2\text{H}_4$  was determined by a colorimetric method using organic probe 3-cyano-7-hydroxycoumarin levulinate (CHCL). CHCL was synthesized according to the literature as shown in Scheme S1.<sup>†</sup><sup>36</sup> Oxalyl chloride (0.82 mL, 8.6 mmol) and DMF (10  $\mu\text{L}$ ) were added to a suspen-





sion of levulinic acid (502 mg, 4.3 mmol) in dichloromethane (50 mL). The reaction mixture was stirred at room temperature for 4 h, and the volatiles were evaporated under reduced pressure and subsequently dried with vacuum pumping. The residue was dissolved in a small amount of dry dichloromethane. The solution was slowly added to the dispersed dichloromethane solution (50 mL) containing 3-cyano-7-hydroxycoumarin (CHC, 284.6 mg, 1.5 mmol) and triethylamine (0.55 mL, 3.9 mmol) at 0 °C. After stirring for 12 h at r.t., the reaction mixture was filtered, and the solution phase was treated with water. The organic phase was separated and washed with 1 mol dm<sup>-3</sup> sodium bicarbonate solution and water and then evaporated to obtain a solid residue. The product was purified by crystallization from dichloromethane and toluene to obtain CHCL. Yield, 18%.

The chromogenic signalling behaviour of CHCL was investigated in a 30% aqueous acetonitrile solution at pH 6.8 (phosphate buffer, 10 mM). CHCL revealed moderate UV-vis absorption at 336 nm. Upon the interaction of CHCL with hydrazine, a prominent absorption band centered at 416 nm developed which is a characteristic of CHC. The changes in absorption bands by the hydrazine-induced deprotection process were used as a ratiometric analysis for the transformation of probe CHCL to CHC.

The calibration curves for NH<sub>3</sub> and N<sub>2</sub>H<sub>4</sub> were shown in Fig. S4.†

## Conclusions

In summary, a two-electrode plasmon-induced NH<sub>3</sub> synthesis system that enables electrical and chemical analysis was fabricated. The bias and pH dependences of the reaction were systematically investigated, and the mechanism of the plasmon-induced NH<sub>3</sub> synthesis on Zr was proposed follow an associative pathway. The results presented herein provide crucial insight into the design of catalysts and electrodes for plasmon-induced NH<sub>3</sub> synthesis. As an aspect of the plasmonic photoanode, higher absorptivity and charge separation efficiency are required to produce a larger number of hot-electrons.

Future studies are aimed at increasing the reaction yield while maintaining high selectivity. The innovative development of the plasmonic photoanode, such as the coupling between plasmons and the other photonic mode, offers enhanced charge separation efficiency.<sup>37,38</sup> Time-resolved measurements of the near and far fields are also important for understanding the plasmon decay and the generation and transportation of the photocarriers.<sup>39–41</sup> Additionally, the development of oxidation co-catalysts is indispensable for quickly consuming the photogenerated holes.<sup>42–44</sup> The development of high-performance cathodes and co-catalysts for nitrogen reduction is also indispensable. Although further improvement of the reaction activity is needed, this robust plasmonic NH<sub>3</sub> synthesis system under visible light irradiation could facilitate the utilization of NH<sub>3</sub> as an energy carrier.

## Conflicts of interest

The authors declare no conflict of interest.

## Acknowledgements

We acknowledge financial support from JSPS KAKENHI (Grant No. JP18H05205, JP17H01041, JP19H02737, JP19H04667, and JP18K05053), the Nanotechnology Platform (Hokkaido University), and the Dynamic Alliance for Open Innovation Bridging Human, Environment and Materials (Five-Star Alliance) of MEXT.

## Notes and references

- 1 L. Green, *Int. J. Hydrogen Energy*, 1982, **7**, 355–359.
- 2 R. Lan, J. T. S. Irvine and S. Tao, *Int. J. Hydrogen Energy*, 2012, **37**, 1482–1494.
- 3 A. Q. Fenwick, J. M. Gregoire and O. R. Luca, *J. Photochem. Photobiol., B*, 2015, **152**, 47–57.
- 4 K. Aika, L. J. Christiansen, I. Dybkjaer, J. B. Hansen, H. Nielsen, A. Nielsen, P. Stoltze and K. Tamaru, *Ammonia*, Springer, Germany, 1995.
- 5 R. Schlögl, *Angew. Chem., Int. Ed.*, 2003, **42**, 2004–2008.
- 6 G. Ertl, *Angew. Chem., Int. Ed.*, 2008, **47**, 3524–3535.
- 7 M. Kitano, Y. Inoue, Y. Yamazaki, F. Hayashi, S. Kanbara, S. Matsuishi, T. Yokoyama, S. W. Kim, M. Hara and H. Hosono, *Nat. Chem.*, 2012, **4**, 934–940.
- 8 M. Kitano, S. Kanbara, Y. Inoue, N. Kuganathan, P. V. Sushko, T. Yokoyama, M. Hara and H. Hosono, *Nat. Commun.*, 2015, **6**, 6731.
- 9 J. Rittle and J. C. Peters, *J. Am. Chem. Soc.*, 2016, **138**, 4243–4248.
- 10 A. R. Singh, B. A. Rohr, J. A. Schwalbe, M. Cargnello, K. Chan, T. F. Jaramillo, I. Chorkendorff and J. K. Nørskov, *ACS Catal.*, 2017, **7**, 706–709.
- 11 D. Bao, Q. Zhang, F. L. Meng, H. X. Zhong, M. M. Shi, Y. Zhang, J. M. Yan, Q. Jiang and X. B. Zhang, *Adv. Mater.*, 2017, **29**, 1604799.
- 12 Y. Yao, S. Zhu, H. Wang, H. Li and M. Shao, *J. Am. Chem. Soc.*, 2018, **140**, 1496–1501.
- 13 G. N. Schrauzer and T. D. Guth, *J. Am. Chem. Soc.*, 1977, **99**, 7189–7193.
- 14 O. Rusina, A. Eremenko, G. Frank, H. P. Strunk and H. Kisch, *Angew. Chem., Int. Ed.*, 2001, **40**, 3993–3995.
- 15 H. Li, J. Shang, Z. Ai and L. Zhang, *J. Am. Chem. Soc.*, 2015, **137**, 6393–6399.
- 16 Y. Lu, Y. Yang, T. Zhang, Z. Ge, H. Chang, P. Xiao, Y. Xie, L. Hua, Q. Li, H. Li, B. Ma, N. Guan, Y. Ma and Y. Chen, *ACS Nano*, 2016, **10**, 10507–10515.
- 17 H. Hirakawa, M. Hashimoto, Y. Shiraishi and T. Hirai, *J. Am. Chem. Soc.*, 2017, **139**, 10929–10936.
- 18 S. Linic, P. Christopher and D. B. Ingram, *Nat. Mater.*, 2011, **10**, 911–921.



- 19 Y. Zhong, K. Ueno, Y. Mori, X. Shi, T. Oshikiri, K. Murakoshi, H. Inoue and H. Misawa, *Angew. Chem., Int. Ed.*, 2014, **53**, 10350–10354.
- 20 M. Ali, F. Zhou, K. Chen, C. Kotzur, C. Xiao, L. Bourgeois, X. Zhang and D. R. MacFarlane, *Nat. Commun.*, 2016, **7**, 11335.
- 21 K. Ueno, T. Oshikiri and H. Misawa, *ChemPhysChem*, 2016, **17**, 199–215.
- 22 C. Li, T. Wang, Z. J. Zhao, W. Yang, J. F. Li, A. Li, Z. Yang, G. A. Ozin and J. Gong, *Angew. Chem., Int. Ed.*, 2018, **57**, 5278–5282.
- 23 J. S. DuChene, G. Tagliabue, A. J. Welch, W. H. Cheng and H. A. Atwater, *Nano Lett.*, 2018, **18**, 2545–2550.
- 24 T. Oshikiri, K. Ueno and H. Misawa, *Angew. Chem., Int. Ed.*, 2014, **53**, 9802–9805.
- 25 T. Oshikiri, K. Ueno and H. Misawa, *Angew. Chem., Int. Ed.*, 2016, **55**, 3942–3946.
- 26 Y. Nishijima, K. Ueno, Y. Kotake, K. Murakoshi, H. Inoue and H. Misawa, *J. Phys. Chem. Lett.*, 2012, **3**, 1248–1252.
- 27 X. Shi, K. Ueno, N. Takabayashi and H. Misawa, *J. Phys. Chem. C*, 2013, **117**, 2494–2499.
- 28 J. L. Ord, *J. Electrochem. Soc.*, 1995, **142**, 879–882.
- 29 M. A. Shipman and M. D. Symes, *Catal. Today*, 2017, **286**, 57–68.
- 30 B. M. Hoffman, D. R. Dean and L. C. Seefeldt, *Acc. Chem. Res.*, 2009, **42**, 609–619.
- 31 T. H. Rod, A. Logadottir and J. K. Nørskov, *J. Chem. Phys.*, 2000, **112**, 5343–5347.
- 32 B. M. Lindley, A. M. Appel, K. Krogh-Jespersen, J. M. Mayer and A. J. M. Miller, *ACS Energy Lett.*, 2016, **1**, 698–704.
- 33 L. J. Kamphake, S. A. Hannah and J. M. Cohen, *Water Res.*, 1967, **1**, 205–216.
- 34 C. Reimann and T. Bredow, *J. Mol. Struct.: THEOCHEM*, 2009, **903**, 89–99.
- 35 E. Skulason, T. Bligaard, S. Gudmundsdottir, F. Studt, J. Rossmeisl, F. Abild-Pedersen, T. Vegge, H. Jonsson and J. K. Nørskov, *Phys. Chem. Chem. Phys.*, 2012, **14**, 1235–1245.
- 36 M. G. Choi, J. Hwang, J. O. Moon, J. Sung and S. K. Chang, *Org. Lett.*, 2011, **13**, 5260–5263.
- 37 X. Shi, K. Ueno, T. Oshikiri, Q. Sun, K. Sasaki and H. Misawa, *Nat. Nanotechnol.*, 2018, **13**, 953–958.
- 38 J. Yang, Q. Sun, K. Ueno, X. Shi, T. Oshikiri, H. Misawa and Q. Gong, *Nat. Commun.*, 2018, **9**, 4858.
- 39 A. Furube, L. Du, K. Hara, R. Katoh and M. Tachiya, *J. Am. Chem. Soc.*, 2007, **129**, 14852–14853.
- 40 Q. Sun, K. Ueno, H. Yu, A. Kubo, Y. Matsuo and H. Misawa, *Light: Sci. Appl.*, 2013, **2**, e118.
- 41 Q. Sun, H. Yu, K. Ueno, A. Kubo, Y. Matsuo and H. Misawa, *ACS Nano*, 2016, **10**, 3835–3842.
- 42 R. D. Smith, M. S. Prevot, R. D. Fagan, S. Trudel and C. P. Berlinguette, *J. Am. Chem. Soc.*, 2013, **135**, 11580–11586.
- 43 A. Iwase, S. Yoshino, T. Takayama, Y. H. Ng, R. Amal and A. Kudo, *J. Am. Chem. Soc.*, 2016, **138**, 10260–10264.
- 44 K. Maeda, K. Ishimaki, Y. Tokunaga, D. Lu and M. Eguchi, *Angew. Chem., Int. Ed.*, 2016, **55**, 8309–8313.

